IEEE Open Journal of the
Industrial Electronics Society

Received 27 November 2025; revised 22 December 2025; accepted 3 January 2026. Date of publication 12 January 2026;
date of current version 22 January 2026. The review of this article was arranged by Associate Editor Binbin Li.

Digital Object Identifier 10.1109/OJIES.2026.3653129

Optimized Modulation for the Four-Switch Buck–Boost Converter With Reduced Current Ripple

VICTOR DIAZ, ANDRES BARRADO (Senior Member, IEEE), PABLO ZUMEL (Member, IEEE), AND ANTONIO LAZARO (Member, IEEE)

Power Electronics Systems Group, Universidad Carlos III de Madrid, 28911 ES Leganés, Spain

CORRESPONDING AUTHOR: VICTOR DIAZ (e-mail: victor.diaz@uc3m.es).

This work was supported in part by the Spanish Ministry of Science, Innovation, and Universities through the research project HIDRON under Grant PID2020-116500RB-I00/AEI/10.13039/501100011033, in part by the European Union-NextGenerationEU/PRTR-C17.I1, the Community of Madrid, and MCIN/AEI/10.13039/501100011033 through the research project GREENH2CM, and in part by PID2021-127707OB-C22 under Grant MICIU/AEI/10.13039/501100011033 and FEDER, UE.

ABSTRACT The four-switch buck–boost converter is a widely used topology due to its bidirectional capability and wide operating voltage range in applications such as battery chargers, photovoltaic applications, or smart grids. This article proposes an improved modulation strategy that reduces the average inductor current, like other state-of-the-art strategies, while also minimizing the inductor's current ripple and the maximum current during the buck–boost operating mode. The objective is to minimize core power losses and reduce conduction power losses in the transistors, thereby improving overall efficiency. To demonstrate this, a state-of-the-art reference modulation strategy is first analyzed. Next, modifications are suggested to obtain the improved strategy, and both are analytically compared. Finally, both modulations are implemented and experimentally validated.

INDEX TERMS DC–DC, four-switch buck–boost (FSBB), modulator, pulsewidth modulation (PWM).

NOMENCLATURE

d_1	Duty cycle switch S_1.
d_2	Duty cycle switch S_2.
IC	Improvement coefficient [A].
I_L	Average inductor current [A].
$i_{L,O}$	Inductor current for the original modulation [A].
$i_{L,P}$	Inductor current for the proposed modulation [A].
$I_{LBB_{\text{boost},O}}$	Average inductor current for the original modulation in the buck–boost region in step-up conditions [A].
$I_{LBB_{\text{boost},P}}$	Average inductor current for the proposed modulation in the buck–boost region in step-up conditions [A].
$I_{LBB_{\text{buck},O}}$	Average inductor current for the original modulation in the buck–boost region in step-down conditions [A].
$I_{LBB_{\text{buck},P}}$	Average inductor current for the proposed modulation in the buck–boost region in step-down conditions [A].
$I_{L_{\max,O}}$	Maximum average current through the inductor for the original modulation [A].
$I_{L_{\max,P}}$	Maximum average current through the inductor for the proposed modulation [A].
$I_{L_{\text{rms},O}}$	Rms current through the inductor for the original modulation [A].
$I_{L_{\text{rms},P}}$	Rms current through the inductor for the proposed modulation [A].
I_{out}	Average output current [A].
M	Static gain.
V_L	Inductor voltage [V].
$V_{car}1$	Carrier signal 1voltage [V].
$V_{car}2$	Carrier signal 2 voltage [V].
V_{in}	Input voltage [V].

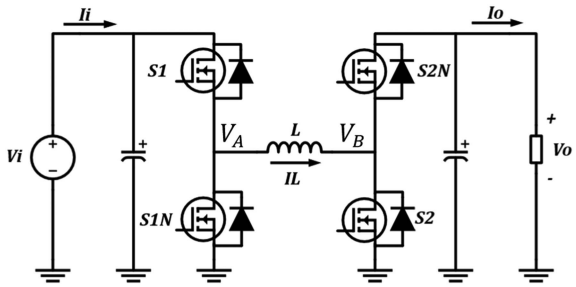

FIGURE 1. Four switch buck–boost converter (FSBB).

V_{mod}	Modulation signal voltage [V].
V_{out}	Output voltage [V].
ZVS	Zero Voltage Switching.
$\Delta i_{L_{BB_{\text{boost},O}}}$	Inductors current ripple for the original modulation in the buck–boost region in step-up conditions [A].
$\Delta i_{L_{BB_{\text{boost},P}}}$	Inductor's current ripple for the proposed modulation in the buck–boost region in step-up conditions [A].
$\Delta i_{L_{BB_{\text{buck},O}}}$	Inductor's current ripple for the original modulation in the buck–boost region in step-down conditions [A].
$\Delta i_{L_{BB_{\text{buck},P}}}$	Inductor's current ripple for the proposed modulation in the buck–boost region in step-down conditions [A].
$\Delta i_{L,\max}$	Maximum current ripple through the inductor [A].
$\Delta i_{L,pu}$	Per unit current ripple through the inductor [A].
ϕ	Phase shift between half bridges.

I. INTRODUCTION

The four-switch buck–boost (FSBB), presented in Fig. 1, is a widely used converter. Its capability to operate over a wide range of input and output voltages makes it appropriate for photovoltaic applications [1], [2], [3], both for achieving bus stability [4], and for maximum power point tracking [5]. This feature, combined with the bidirectionality of the converter, makes it a very suitable option for battery chargers [6], [7], [8] and smart grid applications [9]. Power factor correctors can also be implemented using the FSBB converter [10], [11]. Finally, the electric vehicle industry also relies on this converter for energy management, and hybrid fuel cell electric vehicles [12], [13], [14].

The FSBB works as a synchronous buck converter in series with a synchronous boost converter [15]. This configuration enables operation over a wide range of input and output voltages and bidirectional power transfer. Additionally, this converter reduces the number of components needed, improves overall performance, and reduces the peak transistor current compared to similar dc–dc converters, such as the Cuk converter, the SEPIC, or the nonisolated flyback [5], [11], [16], [17].

The input bridge of the FSBB converter (S_1 and S_{1N}) provides the converter's buck gain. The output bridge (S_2 *and* S_{2N}) supplies the boost gain. The switch S_1 controls the buck gain that commutates with a duty cycle equal to d_1. S_2 controls the boost gain of the converter and switches with a duty cycle equal to d_2. S_{1N} and S_{2N} are driven by complementary signals to S_1 and S_2, respectively. Both d_1 and d_2 depend on the modulation strategy and are smaller than one.

Knowing this, (1) and (2) can be deduced, the average inductor voltage can be represented by (3), and since the average inductor voltage must be equal to zero, the static gain of the converter is given by (4).

The average current through the inductor can be expressed as (5). This equation is only valid if the average current through the inductor during d_2 is equal during $1 - d_2$, which is the case for modulations presented in this article

$$V_A = V_{\text{in}}\, d_1 \tag{1}$$

$$V_B = V_{\text{out}}\ (1 - d_2) \tag{2}$$

$$V_L = V_A - V_B \tag{3}$$

$$M = \frac{V_{\text{out}}}{V_{\text{in}}} = \frac{d_1}{1 - d_2} \tag{4}$$

$$I_L = \frac{I_{\text{out}}}{1 - d_2}. \tag{5}$$

However, (5) cannot be applied for some modulation strategies, such as those that achieve ZVS [18], [19], [20], [21].

It is important to notice that the static gain (4) is not affected by the phase shift ϕ between the bridges driving signals, as will be shown in the following sections. This value does not affect (5), either, meaning the phase shift between bridges can be altered without altering the average output current.

Since the converter has many control variables (i.e., the duty cycle of each bridge, frequency, and phase shift between the bridges), a large number of combinations result in an extensive possibility of compensation of the parameters to be controlled, ideal for optimizing converters.

This converter can be optimized following different strategies. One of the strategies consists of reducing the average current through the inductor (5). In order to minimize (5), d_2 must always be equal to the smallest possible value. To achieve this, whenever the converter is working in step-down mode, d_2 can be set to zero. This implies that the switch S_{2N} is always conducting, so the FSBB would work as a buck converter. Additionally, whenever the FSBB works in a step-up mode, from (4), d_1 must be set to one to minimize the value of d_2. In doing so, S_1 would always be close; thus, the FSBB would work as a boost converter. This strategy generates two modulation modes (2MM), see Fig. 2(a).

This modulation presents some instabilities around $M = 1$, since both control variables d_1 and d_2 are in the boundary conditions. A hysteresis band can be implemented to address this issue, though it significantly increases the output voltage ripple [22].

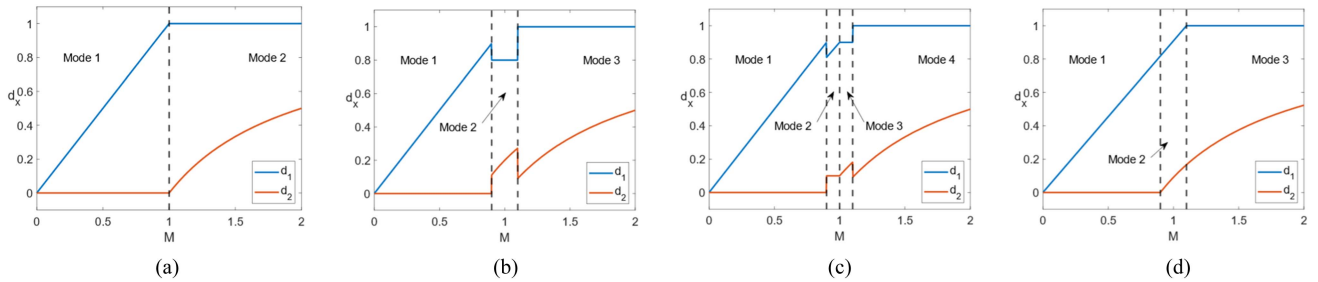

FIGURE 2. d_1 and d_2 in different modulation strategies. (a) 2MM. (b) 3MM. (c) 4MM. (d) ST3MM.

To overcome the limitations of the hysteresis band, the strategy in [23] proposed fixing the duty cycle d_1 to a constant value. While this successfully enforced a single modulation strategy, it introduced a significant drawback: a large increase in the inductor current.

To address this high-current issue, the work in [15] introduced a dedicated buck-boost region, creating a three-modulation-mode (3MM) scheme that also eliminates the hysteresis band. As shown in Fig. 2(b), the control within this new region is achieved by fixing one duty cycle and controlling the converter with the remaining variable.

This concept was further refined in [17], [24], and [25], where it was proposed to split the 3MM buck–boost region into two distinct subregions, thereby creating a four-modulation-mode (4MM) scheme, see Fig. 2(c). The primary benefit of this 4MM approach was to achieve a significant reduction in the average inductor current in the buck–boost region.

These extra regions can control the output voltage for a given gain, but introduce discontinuities when changing from one modulation strategy to another, leading to abrupt changes in the average inductor current. To address these instabilities [26] and [27] implement a modulation with a smooth transition between modes. This smooth transition is achieved by increasing the boost duty cycle (d_2) before the buck duty cycle (d_1) reaches saturation. This creates a smooth transition three-mode-modulation (ST3MM), as shown in Fig. 2(d).

Another important parameter for the study is the inductor's current ripple. This ripple increases power losses and the rms current; therefore, the current ripple should be as small as possible to improve overall efficiency. In [22], a two-edge modulation strategy is presented to reduce the current ripple. This modulation successfully reduces the current ripple but fails to minimize the average current in buck–boost mode and cannot achieve soft transitions between modulation modes.

Finally, in order to improve efficiency, switching losses in the transistors can be reduced by achieving ZVS [18], [19], [20], [21]. These modulation strategies reduce switching losses but increase the rms current through the inductor, increasing conduction losses.

Selecting the modulation can be complex. In [28], all these modulations are analyzed and compared. Based on this analysis, the strategy from [27] was selected as the state-of-the-art reference for this article, primarily because it provides smooth transitions between operating modes without introducing current discontinuities.

TABLE 1. Comparison of Existing Literature and Proposed Work

	Reduce I_L	Soft transition	Reduce Δi_L	Comparison	Study effects of ϕ
[17]	✓			✓	
[22]			✓	✓	
[23]	✓				
[24]	✓				
[25]	✓			✓	
[27]	✓	✓			
[26]	✓	✓			
This work	✓	✓	✓	✓	✓

This article presents a comprehensive optimization of the FSBB modulation strategy, specifically aimed at reducing the inductor current ripple and magnetic stress within the buck–boost region while ensuring soft transitions between operating modes. Building upon the authors' initial analysis in [29], this work uses the phase shift (ϕ) as a free control variable to optimize performance without altering the converter's static gain. Also, it significantly extends the scope of the preliminary analysis and incorporates a study on the phase shift effects, a detailed mathematical derivation of the rms current, and a thorough study of the converter's efficiency.

Consequently, the proposed strategy offers clear advantages over other similar relevant solutions. Unlike the reference soft-transition strategy [27], which ensures mode continuity but neglects ripple optimization, this method significantly minimizes Δi_L and peak currents within the buck–boost region. Additionally, in contrast to other ripple-reduction techniques in [22], it maintains strict operational continuity, avoiding the current discontinuities.

Table 1 compares prior research on the FSBB modulation strategy with the work proposed in this article.

The rest of this article is organized as follows. Section II analyzes the current modulation presented in the state-of-the-art. Section III presents an optimization study on the phase shift between the bridges. The new modulation strategy is analytically exposed and compared to the original in Section IV. In Section V, the converter's efficiency under both modulation strategies is studied. In Section VI, both modulations are implemented and tested in the laboratory, and the experimental results obtained from the tests are compared. Finally, Section VII concludes this article.

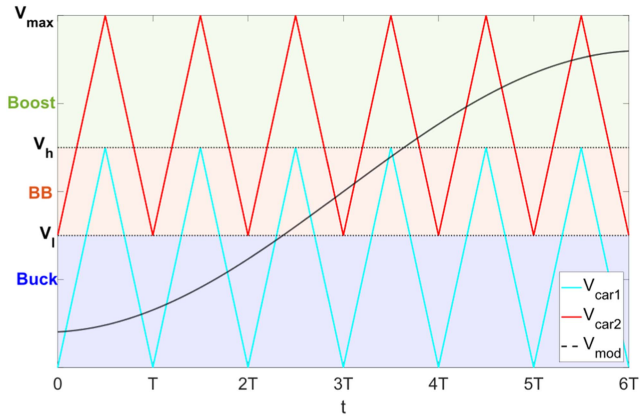

FIGURE 3. Modulation strategy proposed in [26].

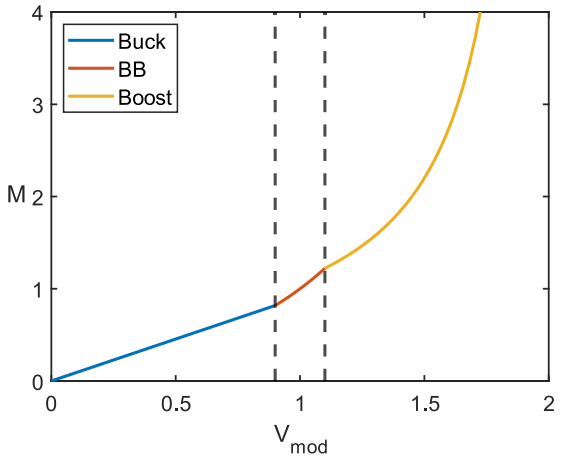

FIGURE 4. Static gain for the three-mode modulation strategy (ST3MM), [26].

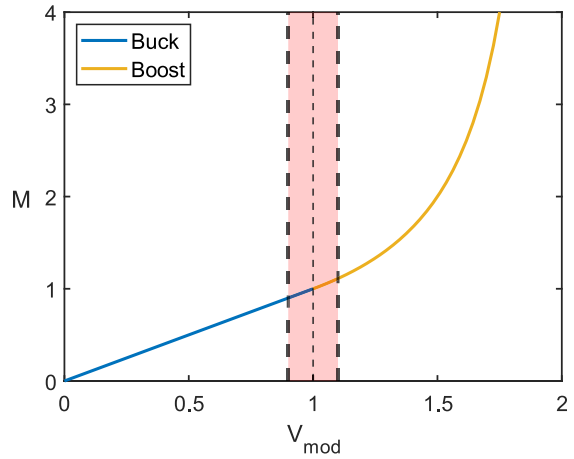

FIGURE 5. Static gain for the buck–boost with 2MM modulation strategy.

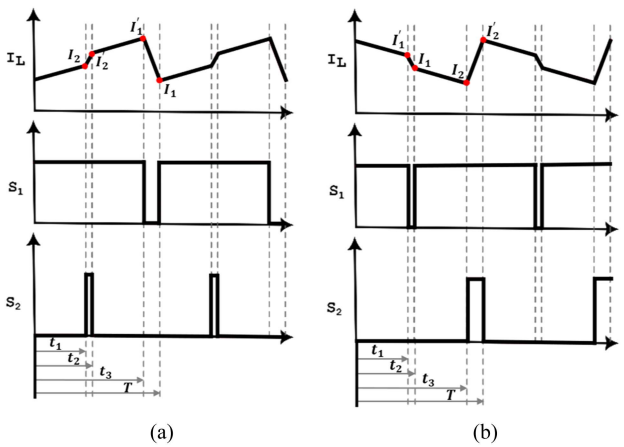

FIGURE 6. Current ripple through the inductor and S_1 and S_2 driver signals in the BB region. (a) Step-down mode. (b) Step-up mode.

II. BUCK–BOOST MODULATION STRATEGY

As mentioned in the previous section, the basic buck–boost modulation strategy with reduced average inductor current presents some instabilities around $M = 1$, since both control variables d_1 and d_2 are in the boundary conditions.

To solve this issue, one of the approaches consists of increasing d_2 before d_1 reaches its maximum value, [26] and [27], creating a third working region.

Two carrier signals are used to implement this modulation, as shown in Fig. 3. The comparison of V_{mod} and V_{car1} commutates the input bridge, whereas the comparison of V_{mod} and V_{car2} controls the output bridge. When the converter works in the buck region ($V_{mod} \leq V_l$), V_{mod} only intersects V_{car1}, switching the first bridge, and since V_{mod} does not cross V_{car2} the output bridge remains fixed. In a similar way, when the converter works in the boost region ($V_{mod} \geq V_h$), the modulator naturally switches the output bridge and maintains the input one fixed. Only when $V_l \leq V_{mod} \leq V_h$ all switches are commutating, and the converter works in the third modulating region.

Adding this extra region modifies the static gain, as shown in Fig. 4, compared with the basic 2MM strategy shown in Fig. 5. In this new region, d_1 and d_2 can then be redefined and expressed as (6) and (7). Based on this information, and considering (4), (9), and (10) can be derived, where $V_{\max}$ corresponds to (8).

The current waveform through the inductor when the converter is operating in this new buck–boost region (BB region), along with the driving signals for S_1 and S_2, are shown in Fig. 6. Analyzing these waveforms, the total current ripple through the inductor can be deduced.

The current ripple formula can be obtained for step-up and step-down modes to ease the study. Note that this does not mean the converter is operating in buck mode (S_2 driven signal must be zero) or boost mode (S_1 driven signal must be one during the entire period); it indicates that it is operating in the buck–boost region, slightly increasing or decreasing the voltages. The total current ripple in step-down conditions is equal to (11) and represents $I_1' - I_1$, Fig. 6

$$d_1 = \frac{V_{mod}}{V_h} \tag{6}$$

$$d_2 = \frac{V_{mod} - V_l}{V_h} \tag{7}$$

$$V_{\max} = V_h + V_l \tag{8}$$

$$M = \frac{V_{\text{out}}}{V_{\text{in}}} = \frac{V_{mod}}{V_{\max} - V_{mod}} \tag{9}$$

$$V_{mod} = V_{\max}\frac{M}{1+M}. \tag{10}$$

Equivalently, the total current ripple in step-up is equal to (12) and represents $I_2' - I_2$. These expressions correspond to the original modulation referenced with subindex "O"

$$\Delta i_{L_{BB_{\text{buck},O}}} = \frac{V_{\text{out}}\,(1-d_1)\,T}{L} = \frac{V_{\text{out}}\,(V_h\,V_{\text{in}} - V_l\,V_{\text{out}})}{L\,f\,V_h\,\,(V_{\text{in}}+V_{\text{out}})} \tag{11}$$

$$\Delta i_{L_{BB_{\text{boost},O}}} = \frac{V_{\text{in}}\,d_2\,T}{L} = \frac{V_{\text{in}}\,(V_h\,V_{\text{out}} - V_l\,V_{\text{in}})}{L\,f\,V_h\,\,(V_{\text{in}}+V_{\text{out}})}. \tag{12}$$

In order to analyze the maximum current value, the average current, I_L is computed, (15) and (16), following (13) and knowing that the current through the inductor $i_{L,O}(t)$ can be expressed as (14) according to Fig. 6

$$I_L = \frac{1}{T}\int_0^T i_L\,(t)\;dt \tag{13}$$

$$i_{L,O}\,(t) = \begin{cases} I_1 + \frac{(V_{\text{in}}-V_{\text{out}})\,t}{L}, & t < t_1 \\ I_2 + \frac{V_{\text{in}}\,(t-t_1)}{L}, & t_1 < t < t_2 \\ I_2' + \frac{(V_{\text{in}}-V_{\text{out}})\,(t-t_2)}{L}, & t_2 < t < t_3 \\ I_1' - \frac{V_{\text{out}}\,(t-t_3)}{L}, & t_3 < t < T \end{cases} \tag{14}$$

$$I_{LBB_{\text{buck},O}} = I_1 + \frac{V_{\text{out}}\,(V_h V_{\text{in}} - V_l V_{\text{out}})}{2LfV_h\,(V_{\text{in}}+V_{\text{out}})} \tag{15}$$

$$I_{L_{BB_{\text{boost},O}}} = I_2 + \frac{V_{\text{in}}\,(V_h V_{\text{out}} - V_l V_{\text{in}})}{2LfV_h\,(V_{\text{in}}+V_{\text{out}})}. \tag{16}$$

Analyzing the average current through the inductor, (15) and (16), the current ripple for this modulation, (11) and (12), and Fig. 6, it can be stated that for both scenarios, buck mode and boost mode in the BB region, the maximum inductor current is

$$I_{L_{\max},O} = I_{L,O} + \frac{\Delta i_{L,O}}{2}. \tag{17}$$

III. PHI OPTIMIZATION

As pointed out in the introduction, (4) does not depend on the phase shift between the bridge's driving signals, ϕ. Considering this, the main aim of this article is to reduce the current ripple by changing this parameter. A general approach to this optimization is illustrated in Fig. 7.

The proposed phase-shifted modulation strategy has a ripple characteristic that is highly dependent on the phase angle, ϕ. This analysis reveals two distinct regions of operation based on whether the carrier signals overlap. When the phase shift ϕ is below a specific threshold, the two carrier signals do not intersect. In this nonoverlapping region, our analysis shows that the current ripple remains constant and identical to that produced by the original, nonshifted modulation (11) and (12).

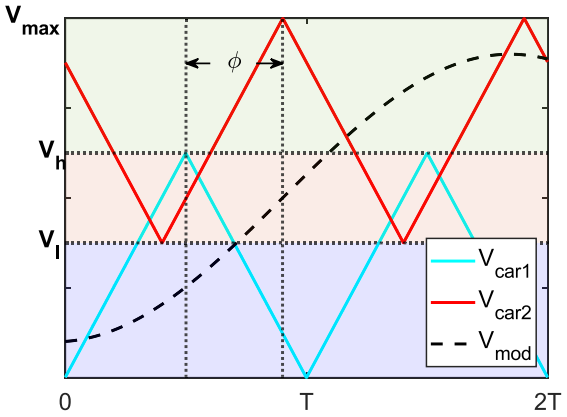

FIGURE 7. Modulation strategy depending on the phase shift with an overlapping region.

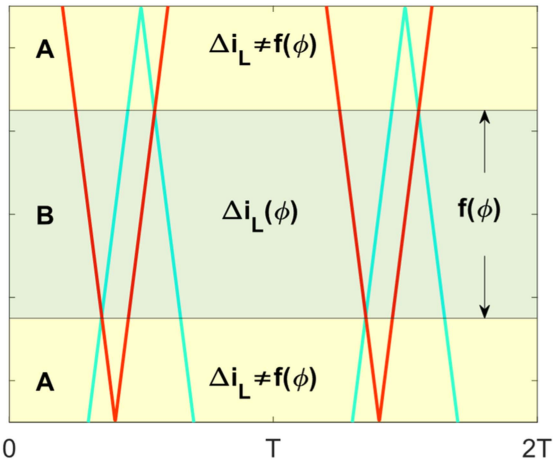

FIGURE 8. Extra regions in the buck–boost operating mode.

However, as ϕ increases beyond this threshold, the two carrier signals begin to overlap, see Fig. 7. In this overlapping region, the analysis shows that the current ripple is no longer constant; it begins to vary and decrease as the phase shift increases.

The boundary between these two regions is therefore a critical parameter. Equation (18) defines this exact boundary condition: the minimum phase shift required for the carriers to make initial contact. This equation was derived graphically, by using the line equations of the carrier waveforms to analytically solve for the precise angle ϕ at which they first intersect. Finally, due to the symmetrical properties of the carriers, the full spectrum of this behavior can be understood by limiting the study to the range $\phi \in [0,\ 180]$

$$\phi_{\min} = 180\,\frac{V_l}{V_h}. \tag{18}$$

Once ϕ exceeds the minimum value, the buck–boost operating mode is itself divided into two new subregions, as illustrated in Fig. 8. Equation (19) defines the specific threshold for the modulating signal that separates these two new

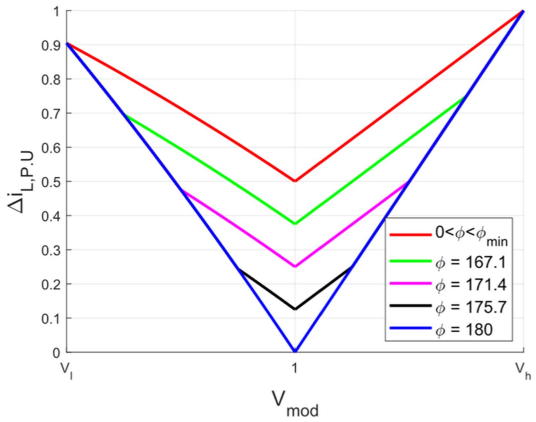

FIGURE 9. Current ripple in the BB region with respect to ϕ.

modes

$$V_{mod} = \frac{V_{\max}}{2} \pm V_h \frac{180 - \phi}{360}. \tag{19}$$

These two new operating regions exhibit distinct ripple characteristics. In the first region (A), the current ripple is independent of ϕ, as described by (20) and (21). In the second region (B), however, the ripple becomes directly dependent on the phase shift between the bridges, as governed by (22) and (23).

Notice that these equations are only valid when $\phi \in [\phi_{\min}, 180]$. These equations analytically demonstrate that as the phase shift ϕ increases, the current ripple decreases. Fig. 9 graphically illustrates the inductor current ripple as a function of the phase shift

$$\Delta i_{L_{BB_{\text{buck},A}}} = \frac{V_{\text{out}}\, V_{\max}\, (V_{\text{in}} - V_{\text{out}})}{L\, f\, V_h\, (V_{\text{in}} + V_{\text{out}})} \tag{20}$$

$$\Delta i_{L_{BB_{\text{boost},A}}} = \frac{V_{\text{in}}\, V_{\max}\, (V_{\text{out}} - V_{\text{in}})}{L\, f\, V_h\, (V_{\text{in}} + V_{\text{out}})} \tag{21}$$

$$\Delta i_{L_{BB_{\text{buck},B}}} = \frac{V_{\text{out}}}{L\, f} \left(\frac{V_{\max}\, (V_{\text{in}} - V_{\text{out}})}{2\, V_h\, (V_{\text{in}} + V_{\text{out}})} + \frac{180 - \phi}{360} \right) \tag{22}$$

$$\Delta i_{L_{BB_{\text{boost},B}}} = \frac{V_{in}}{L\, f} \left(\frac{V_{\max}\, (V_{\text{out}} - V_{\text{in}})}{2\, V_h\, (V_{\text{in}} + V_{\text{out}})} + \frac{180 - \phi}{360} \right). \tag{23}$$

IV. PROPOSED MODULATION STRATEGY

As studied in the previous section, the phase shift that minimizes the current ripple is 180°. Therefore, the improvement proposed by the new modulation strategy consists of fixing ϕ at 180°, which is equivalent to shifting one of the carrier signals 180° with respect to the other, as shown in Fig. 10.

This modification does not affect the static gain for this modulation, see Fig. 4, or the limits between the different modulation modes. This change only affects the current ripple.

The new current waveform through the inductor is shown in Fig. 11, both in step-up and step-down conditions. Based on this new waveform, the new ripple current can be expressed as

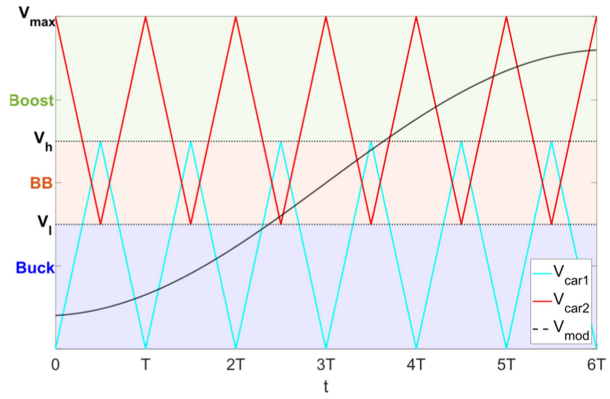

FIGURE 10. Proposed modulation strategy shifting the carrier signal 180°.

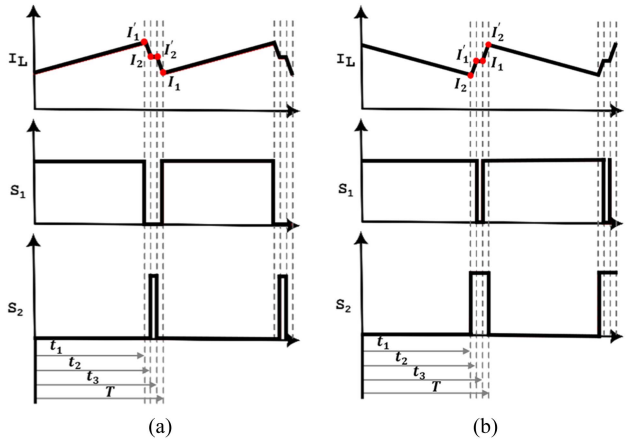

FIGURE 11. Current ripple through the inductor for the proposed modulation strategy and *S1* and *S2* driven signals in the BB region. (a) Step-down mode. (b) Step-up mode.

(24) and (25). These expressions correspond to the proposed modulation referenced with subindex "P".

As in the previous case, in order to analyze the maximum current value, the current's average value is computed. Analyzing the waveforms in Fig. 11, (26) and (27) can be obtained. In this modulation, two equations are needed to describe the current through the inductor since the edges of the control signals cross each other and modify the sequence of current values ($I_1^{'}, I_2,\ I_2^{'},\ I_1$ in step-down mode, and $I_2,\ I_1^{'},\ I_1,\ I_2^{'}$ in step-up mode). With these equations and knowing (13), (28), and (29) can be computed.

As in the previous modulation, knowing the average current and the current ripple (28) and (29), and (24) and (25), respectively, and the current waveform in Fig. 11, it can be stated that for both scenarios, the maximum inductor current is equivalent to (30)

$$\Delta i_{LBB_{\text{buck},P}} = \frac{V_{\text{out}}\,(1 - d_1 - d_2)\,T}{L} = \frac{V_{\text{out}}\, V_{\max}\, (V_{\text{in}} - V_{\text{out}})}{L\, f\, V_h\, (V_{\text{in}} + V_{\text{out}})} \tag{24}$$

$$\Delta i_{LBB_{\text{boost},P}} = \frac{V_{\text{in}}\,(d_2 - 1 + d_1)\,T}{L} = \frac{V_{\text{in}}\,V_{\max}\,(V_{\text{out}} - V_{\text{in}})}{L\,f\,V_h\,(V_{\text{in}} + V_{\text{out}})} \tag{25}$$

$$i_{L,P}(t) = \begin{cases} I_1 + \frac{(V_{\text{in}} - V_{\text{out}})\,t}{L}, & t < t_1 \\ I_1' - \frac{V_{\text{out}}\,(t - t_1)}{L}, & t_1 < t < t_2 \\ I_2, & t_2 < t < t_3 \\ I_2 - \frac{V_{\text{out}}\,(t - t_3)}{L}, & t_3 < t < T \end{cases} \tag{26}$$

$$i_{L,P}(t) = \begin{cases} I_2' + \frac{(V_{\text{in}} - V_{\text{out}})\,t}{L}, & t < t_1 \\ I_2 + \frac{V_{\text{in}}\,(t - t_1)}{L}, & t_1 < t < t_2 \\ I_1', & t_2 < t < t_3 \\ I_1 + \frac{V_{\text{in}}\,(t - t_3)}{L}, & t_3 < t < T \end{cases} \tag{27}$$

$$I_{L_{BB_{\text{buck},P}}} = I_1 + \frac{V_{\text{out}} V_{\max}\,(V_{\text{in}} - V_{\text{out}})}{2LfV_h\,(V_{\text{in}} + V_{\text{out}})} \tag{28}$$

$$I_{L_{BB_{\text{boost},P}}} = I_2 + \frac{V_{in} V_{\max}\,(V_{\text{out}} - V_{\text{in}})}{2LfV_h\,(V_{\text{in}} + V_{\text{out}})} \tag{29}$$

$$I_{L_{\max},P} = I_{L,P} + \frac{\Delta i_{L,P}}{2}. \tag{30}$$

According to (17) and (30), and since (5) is satisfied for both modulations, it can be deduced that the modulation with the smallest current ripple will deliver the lowest maximum current.

Furthermore, it is critical to note that the expressions for the average inductor current and the duty cycles are not modified by this optimization. Since these equations remain unchanged, the averaged models for both the original and the proposed modulations are equivalent. Consequently, the small-signal transfer function is also identical, and the system's dynamic response remains unaffected by the proposed optimization.

Comparing (11) and (24) related to the current ripple in buck mode, it can be noticed that the new modulation reduces the current ripple in step-down conditions whenever (32) is met, i.e., always

$$\frac{V_{\text{out}}\,(1 - d_1)\,T}{L} \geq \frac{V_{\text{out}}\,(1 - d_1 - d_2)\,T}{L} \tag{31}$$

$$d_2 \geq 0. \tag{32}$$

Additionally, comparing the ripple in step-up conditions for both modulations (12) and (25), it can also be checked that the proposed method reduces the current ripple in all cases (34)

$$\frac{V_{\text{in}}\,d_2\,T}{L} \geq \frac{V_{\text{in}}\,(d_2 - (1 - d_1))\,T}{L} \tag{33}$$

$$d_1 \leq 1. \tag{34}$$

These conclusions can also be verified by graphing the (11), (12), (24), and (25). These equations depend on the frequency of the PWM signal ($f = 1/T$) and the inductance (L). It means that, even though the ripple current is always smaller under the proposed modulation, depending on these two parameters, L and T, the absolute value of this reduction varies. Fig. 12 plots the relationship defined in (41), which represents the inductor current ripple normalized against its maximum possible value. This maximum ripple, defined in (40), occurs at the condition $V_{mod} = V_h$

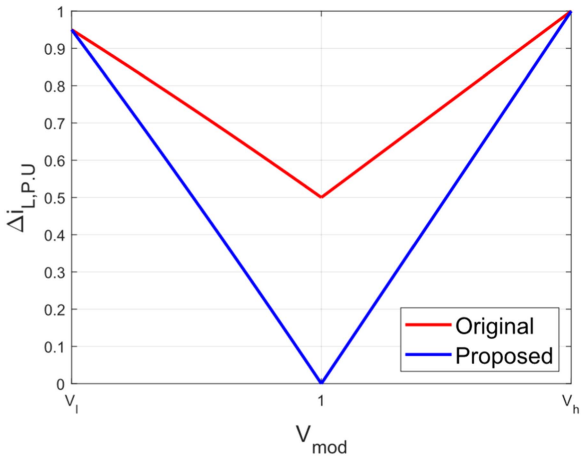

FIGURE 12. Current ripple value per unit in the BB region (V_l=0.95; V_h=1.05).

$$\Delta i_{L,\max} = \frac{V_{\text{in}}\,(V_h - V_l)}{L\,f\,V_h} \tag{40}$$

$$\Delta i_{L,pu} = \frac{\Delta i_L}{\Delta i_{L,\max}} = \frac{\Delta i_L\,L\,f\,V_h}{V_{\text{in}}\,(V_h - V_l)}. \tag{41}$$

It can be observed that the relative improvement over the original is greater the closer to $V_{\text{in}} = V_{\text{out}}$, i.e., V_{mod} equal to one. However, the absolute value of the current ripple is very dependent on the inductance and frequency. It can also be appreciated that the new modulation reduces the current ripple to zero as long as V_{mod} is equal to one.

Given that the proposed modulation does not affect the static gain (4) nor the values of d_1 or d_2, it can be stated that, according to (5), the average current through the inductor will remain the same as in the original modulation.

Since the average value is the same in both modulators and, as shown, the ripple is smaller under the new modulation strategy, the proposed modulation also reduces the peak value of the current through the inductor according to (17) and (30).

Finally, the rms value for both modulations is analyzed. The general formula for rms current is presented in (42). Computing this formula on (14), (26), and (27), the rms values for each modulation are obtained (35), (36), and (37) shown at the bottom of the next page. These equations are further expanded in the appendix

$$I_{L_{\text{rms}}}^2 = \frac{1}{T}\int_0^T i_L(t)^2\,dt. \tag{42}$$

Comparing the rms values, an improvement coefficient "*IC*" (43) can be obtained, as shown in (38) and (39) shown at the bottom of the next page

$$IC = I_{L_{\text{rms},O}}^2 - I_{L_{\text{rms},P}}^2. \tag{43}$$

By analyzing (38) and (39), knowing that all ripple values are positive, that the proposed modulation ripple is always

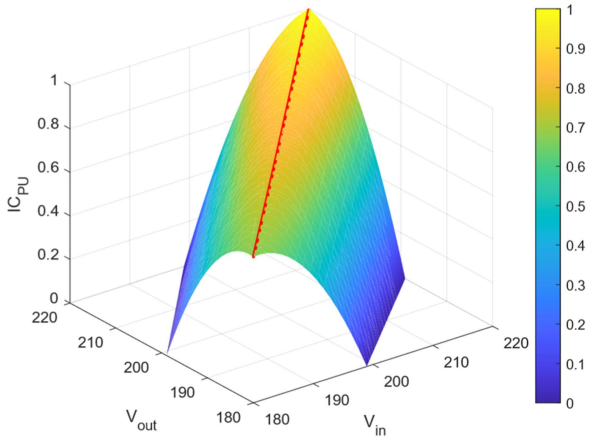

FIGURE 13. Normalized rms current improvement with respect to input and output voltages, 3-D (maximum improvement highlighted in red).

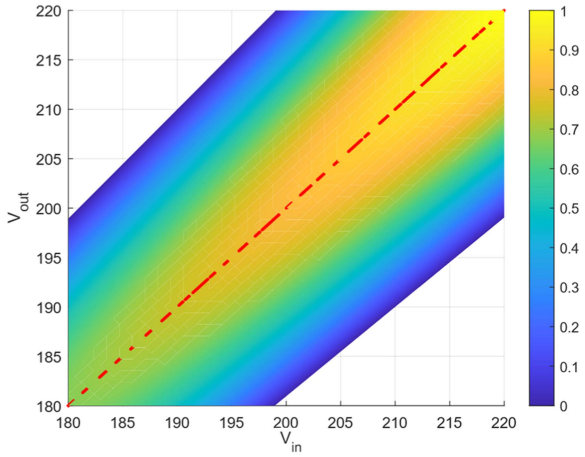

FIGURE 14. Normalized rms current improvement with respect to input and output voltages, 2-D (maximum improvement highlighted in red).

smaller than the original, and that $d_1 > d_2$, it can be stated that the proposed modulation always reduces the rms value of the current through the inductor.

From (38) and (39), it can be deduced that the maximum improvement for any given input voltage occurs when the current ripple difference is maximum, i.e., when M = 1. Additionally, knowing (40), it can be stated that the greater V_{in} the greater the absolute current ripple difference.

To quantify the improvement, we introduce the normalized improvement coefficient (IC_{PU}), which is defined in (46). This coefficient represents the rms current difference normalized by the maximum rms difference value, and it is plotted in Figs. 13 and 14.

The maximum value of this coefficient (IC_{max}) occurs when the current ripple difference is at its highest. Based on (40), this condition is met when the input voltage is at its maximum, and input and output voltages are equal ($M = 1$), as observed in Fig. 12, (44) and (45).

By analyzing the resulting surface, it can be concluded that the maximum improvements occur when $M = 1$ (highlighted in red in both figures). This maximum improvement can be computed as (47).

$$IC_{\text{max}} = IC\,|_{M=1,V_{\text{in}}=V_{\text{in,max}}} \tag{44}$$

$$IC_{\text{max}} = \frac{V_{\text{in,max}}^2\,\left(V_h^3 - 3\,V_l^2 V_h + 2\,V_l^3\right)}{48\,L^2\,f^2\,V_h^3} \tag{45}$$

$$IC_{PU} = \frac{IC}{IC_{\text{max}}}. \tag{46}$$

This result also allows us to know how this improvement evolves. For constant output power and gain, the higher the voltage, the greater the improvement, since ripple increases with voltage

$$IC\,|_{V_{\text{in}}=V_{\text{out}}} = \frac{\Delta i_{L,O}^2\;(1+2\;(V_l/V_h))}{12}. \tag{47}$$

V. EFFICIENCY

In order to study the converter's efficiency, the power losses are analyzed. This chapter analyzes whether the converter's efficiency improves under the proposed modulation.

$$I_{L_{\text{rms},O}}^2 = I_L^2 + \frac{\Delta i_{L_{BB_{\text{buck},O}}}^2\,(1-d_2)}{12} + \frac{\Delta i_{L_{BB_{\text{boost},O}}}^2\,d_1}{12} + \frac{\Delta i_{L_{BB_{\text{buck},O}}}\,\Delta i_{L_{BB_{\text{boost},O}}}\,(d_1-d_2)}{12} \tag{35}$$

$$I_{L_{\text{rms},P}}^2 = I_L^2 + \frac{\Delta i_{L_{BB_{\text{buck},P}}}^2\,(1-d_2)}{12} \quad \textbf{if } \boldsymbol{V_{\text{in}} \geq V_{\text{out}}} \tag{36}$$

$$I_L^2 + \frac{\Delta i_{L_{BB_{\text{boost},P}}}^2\,d_1}{12} \quad \text{if } \boldsymbol{V_{\text{in}} \leq V_{\text{out}}} \tag{37}$$

$$IC = \frac{\left(\Delta i_{L_{BB_{\text{buck},O}}}^2 - \Delta i_{L_{BB_{\text{buck},P}}}^2\right)(1-d_2)}{12} + \frac{\Delta i_{L_{BB_{\text{boost},O}}}^2\,d_1}{12} + \frac{\Delta i_{L_{BB_{\text{buck},O}}}\,\Delta i_{L_{BB_{\text{boost},O}}}\,(d_1-d_2)}{12} \quad \textbf{if } \boldsymbol{V_{\text{in}} \geq V_{\text{out}}} \tag{38}$$

$$\frac{\Delta i_{L_{BB_{\text{buck},O}}}^2\,(1-d_2)}{12} + \frac{\left(\Delta i_{L_{BB_{\text{boost},O}}}^2 - \Delta i_{L_{BB_{\text{boost},P}}}^2\right)d_1}{12} + \frac{\Delta i_{L_{BB_{\text{buck},O}}}\,\Delta i_{L_{BB_{\text{boost},O}}}\,(d_1-d_2)}{12} \quad \textbf{if } \boldsymbol{V_{\text{in}} \leq V_{\text{out}}} \tag{39}$$

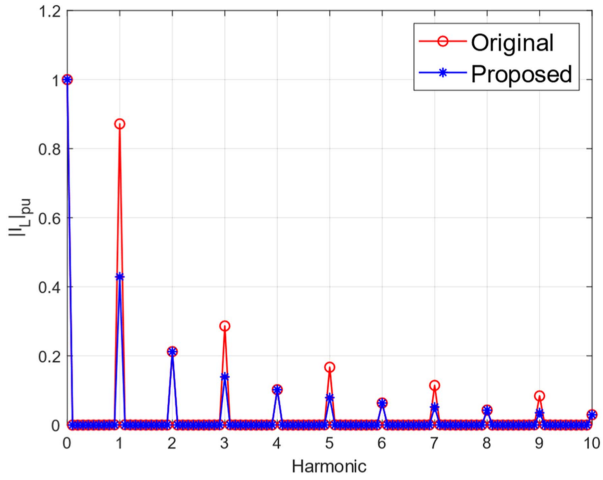

FIGURE 15. Inductor current harmonic distribution depending on the modulation strategy.

A. INDUCTOR

The inductor losses can be separated into copper losses and core losses. Copper losses correspond to the dissipated power in the inductor conductor. An approximation to these losses is given in

$$P_{CU} = I_{L_{\text{rms}}}^2 \, r_L \tag{48}$$

where r_L corresponds to the inductor's wire resistance in dc. This approximation indicates that the lower the $I_{L_{\text{rms}}}$ the lower the losses will be. As seen in the previous section, the proposed modulation always reduces the rms current through the inductor, thus, the copper losses will always be reduced. However, (48) is an approximation. In [30] and [31], a more precise computation of these losses is presented.

In these papers, the inductor resistance is computed for each harmonic of the inductor current

$$P_{CU} = \sum_{n=0}^{\infty} I_{L,n_{\text{rms}}}^2 \, r_{ac,n} \tag{49}$$

where $I_{L,n_{\text{rms}}}$ corresponds to the rms value of the nth harmonic of the current through the inductor and $r_{ac,n}$ to the corresponding resistance for those harmonics.

Computing the fast Fourier transform of the inductor current, Fig. 15, it can be observed that the proposed modulation reduces odd harmonics, thereby reducing power losses.

The core losses must also be considered in the inductor. These losses correspond to the power dissipated in the inductor core. These losses can be approximated using the Steinmetz (50). This equation already indicates the relationship between the different parameters and the losses

$$P_{\text{core}} = K \, \hat{B}^{\beta} \, A_c \, l_m \tag{50}$$

where K and β are parameters that depend on the core material, and A_c and l_m to the core geometry. The only parameter that varies depending on the modulation is $\hat{B}$, according to the following formula:

$$\hat{B} = \frac{\Delta B}{2} = \frac{L \, \Delta i}{2 \, n \, A_e}. \tag{51}$$

Since, n, L, and A_e are also dependent on the inductor design, the modulation strategy can only vary Δi. As seen in the previous section, Δi under the proposed modulation is always smaller; therefore, the core losses will always be smaller.

B. TRANSISTORS

As in the inductor case, the transistor losses can be divided into switching and conduction losses. The conduction losses can be expressed as follows:

$$P_{cond} = I_{S_{\text{rms}}}^2 \, R_{DS,\text{on}} \tag{52}$$

where $R_{DS,\text{on}}$ corresponds to the parasitic resistor of the transistor when it is in conduction. Therefore, the conduction losses in the converter, assuming all transistors are equal, can be expressed as

$$P_{cond} = R_{DS} \left(I_{S1_{\text{rms}}}^2 + I_{S1N_{\text{rms}}}^2 + I_{S2_{\text{rms}}}^2 + I_{S2N_{\text{rms}}}^2 \right). \tag{53}$$

If the converter is analyzed from Fig. 1

$$I_{L_{\text{rms}}}^2 = I_{S1_{\text{rms}}}^2 + I_{S1N_{\text{rms}}}^2 = I_{S2_{\text{rms}}}^2 + I_{S2N_{\text{rms}}}^2. \tag{54}$$

Therefore, the converter's conduction losses, according to (53) and (54), can be expressed as

$$P_{cond} = 2 \, I_{L_{\text{rms}}}^2 \, R_{DS,\text{on}}. \tag{55}$$

As shown in the previous section, the proposed modulation always reduces the rms current through the inductor; thus, the transistors' conduction losses in the converter are always smaller.

For the transistors' switching losses, the following formula applies:

$$P_{SW} = \frac{1}{2} \, f \, V_{DS} \, \left(t_{\text{turnon}} \, I_{\text{on}} + t_{\text{turnoff}} \, I_{\text{off}} \right). \tag{56}$$

Being f the switching frequency of the converter, V_{DS} the blocking voltage the transistor withstands, I_{on} and I_{off} the current when the transistors turn ON and OFF, and finally, t_{turnon} and t_{turnoff} the time required to fully change states. Since both transistors in a branch switch simultaneously, the currents can be considered equal. Knowing this information for this specific converter and the specific currents shown in Figs. 6 and 11, it can be stated that

$$P_{S1sw} + P_{S1Nsw} = \frac{f}{2} \, V_{\text{in}} \left(t_{\text{turnon}} + t_{\text{turnoff}} \right) \left(I_1 + I_1^{'} \right) \tag{57}$$

$$P_{S2sw} + P_{S2Nsw} = \frac{f}{2} \, V_{\text{out}} \left(t_{\text{turnon}} + t_{\text{turnoff}} \right) \left(I_2 + I_2^{'} \right). \tag{58}$$

Nevertheless, if the deadtime is big enough, switches S_{1N} and S_{2N} can have soft switching at both turn-ON and turn-OFF, meaning (57) and (58) do not apply to this specific case, and that switching losses in these transistors are negligible.

Consequently, the total switching losses can be expressed as the sum of the switching losses on transistors S_1 and S_2

$$P_{S1sw} = \frac{1}{2} f V_{in} \left(t_{\text{turnon}} I_1 + t_{\text{turnoff}} I_1^{'} \right) \tag{59}$$

$$P_{S2sw} = \frac{1}{2} f V_{\text{out}} \left(t_{\text{turnon}} I_2 + t_{\text{turnoff}} I_2^{'} \right). \tag{60}$$

The proposed modulation reduces the current ripple while simultaneously maintaining the average current value. Consequently, it can be deduced that the current peak value will be reduced, thereby improving switching losses. However, as seen in Figs. 6 and 11, the minimum value will increase by the same amount, thereby increasing power losses.

The peak current improvement with the proposed modulation ($I_{1,O} - \mathrm{I}_{1,P} = \Delta I_1$ in step-down conditions or $I_{2,O} - \mathrm{I}_{2,P} = \Delta I_2$ in step-up) will be equal to the increase in the minimum current ($I_{1,O}^{'} - \mathrm{I}_{1,P}^{'} = -\Delta I_1$ in step-down conditions or $I_{2,O}^{'} - \mathrm{I}_{2,P}^{'} = -\Delta I_2$ in step-up). Therefore, the difference between modulations can be expressed as

$$\Delta P_{S1sw,O} - \Delta P_{S1sw,P} = \frac{1}{2} f V_{\text{in}} \Delta I_1 \left(t_{\text{turnon}} - t_{\text{turnoff}} \right) \tag{61}$$

$$\Delta P_{S2sw,O} - \Delta P_{S2sw,P} = \frac{1}{2} f V_{\text{out}} \Delta I_2 \left(t_{\text{turnon}} - t_{\text{turnoff}} \right). \tag{62}$$

In this case, the total switching losses depend on the times t_{turnon} and t_{turnoff}. If $t_{\text{turnon}} = t_{\text{turnoff}}$ the switching losses will then remain constant. If $t_{\text{turnon}} < t_{\text{turnoff}}$ the switching losses will be smaller under the new modulation strategy. Finally, if $t_{\text{turnon}} > t_{\text{turnoff}}$ for the proposed modulation, the switching losses will increase.

Finally, the energy stored in the MOSFET's parasitic capacitors (C_{OSS}) can also be considered in the switching losses. Since the proposed modulation does not affect the converter's operating region, the losses will remain constant.

After studying the converter's efficiency, it has been proven that the inductor losses and the transistor conduction losses diminish in all cases under the proposed modulation strategy, as a direct result of the reduced inductor rms current. The transistors' switching losses, however, depend heavily on the specific component selection.

For this reason, the final loss distribution is highly tied to the specific transistor selection and inductor design. The overall efficiency improvement should therefore be studied for each unique scenario, although the guaranteed reduction of both inductors and conduction losses will initially favor the new modulation.

VI. IMPLEMENTATION AND EXPERIMENTAL RESULTS

Several tests are carried out in the laboratory to compare efficiency and the converter's inductor current ripple under different modulation strategies.

The first step in implementing the new modulation is to generate the phase shift between the two carrier signals. For the traditional modulation strategy, the generation of the second carrier signal is simple; the value of V_l must be added to the generated triangular signal (63).

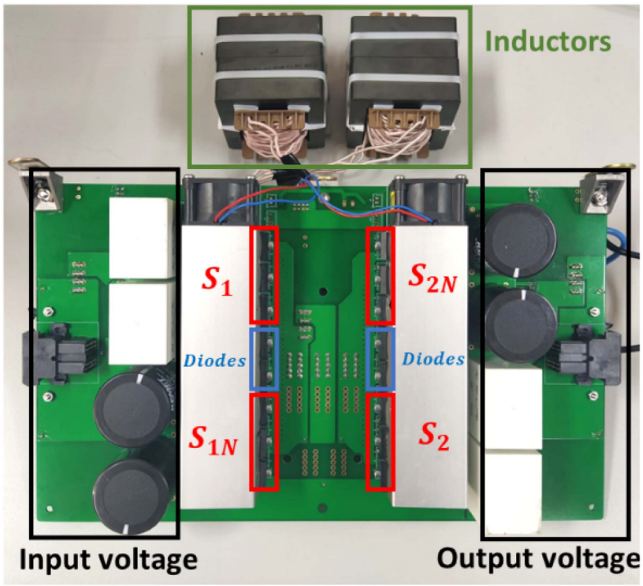

FIGURE 16. FSBB converter implemented in the laboratory.

For the new modulation, this equation must be modified, where the new carrier signal is now computed as V_{max} minus the original triangular signal (64). It introduces a 180° phase shift between the two bridges with a very simple modification to the original

$$V_{car2} = V_{car1} + V_l \tag{63}$$

$$V_{car2} = V_{\text{max}} - V_{car1}. \tag{64}$$

The smaller the buck–boost region, the higher the converter's efficiency, since there are fewer operating conditions in which all transistors are switching. This region must also be big enough to avoid instabilities around $M = 1$.

Since (4) does not depend on ϕ, and the gain of the proposed modulation is equivalent to the original, this is the only modification needed to implement the new modulation strategy. The control stage, feedforward (if implemented), and other control elements in the previous modulator remain unchanged.

The modulator and the corresponding protections have been digitally implemented in a SoC (ZedBoard) to perform the tests. All system parameters are acquired using a PmodAD1, a 12-bit analog-to-digital converter.

A general-purpose test platform designed by the company Power Smart Control S.L. (SmartRPP by PSC) has been used for the power converter. For the converter's switches, three SCT3022AL MOSFETS are implemented in parallel, with an FFSH5065A-F155 Schottky diode in antiparallel, Fig. 16. The maximum converters voltage is 600 V, with a maximum frequency of 500 kHz and a maximum power of 20 kW.

TABLE 2. Test Main Specifications

V_{in}	200 V
V_{out}	195 V − 205 V
P_{out}	1 − 5 kW
f	100 kHz
L	3.7 μH

A small inductance of 3.7 μH (implemented with two parallel 7.4 μH inductors) has been selected to ease the current ripple study.

To perform the experiments, both modulations have been tested under various conditions: step-up mode, step-down mode, equal input and output voltages, and a wide power range, as indicated in Table 2.

The switching frequency was set to 100 kHz. This value was selected for the original modulation to achieve low current ripple with reasonably sized passive components. This frequency was kept constant for both the original and the proposed strategies to ensure a fair and direct comparison. This allows the performance improvements shown in the results to be attributed directly to the modulation strategy itself, rather than to a change in frequency.

The specific power range was selected as it corresponds to the nominal design specifications of the experimental prototype and the capabilities of the available load bank. It is important to clarify that this range reflects the tested nominal boundaries of the hardware, not a fundamental limitation of the proposed modulation strategy, which remains fully functional and stable down to zero power conditions due to its inherent bidirectional nature.

Finally, the comparative analysis is intentionally focused on the buck–boost operating region. This is because the core contribution of this work, related to the optimized phase-shift, only affects the buck–boost region. In the pure buck or pure boost regions, both the original and the proposed modulation strategies converge and operate identically. Therefore, focusing the analysis on the buck–boost region is essential to properly isolate and validate the benefits of our proposed method. The test conditions for the experimental results are listed in Table 2.

Under these conditions, the ripple was studied and compared with theoretical computations. Fig. 17 shows the results of the experiments. This figure plots the inductor current ripple, where the solid lines represent the theoretically predicted values from the analytical model, and the discrete markers ("∗" and "o") represent the actual ripple values measured from the experimental prototype.

As shown, the measured experimental ripple values closely track the predicted analytical curves for both the original (O) and proposed (P) methods. This demonstrates an excellent agreement, with a maximum observed deviation of less than 7%. This minor and expected deviation is primarily due to parasitic elements (such as parasitic resistances and switch nonidealities) that were not included in the simplified analytical model.

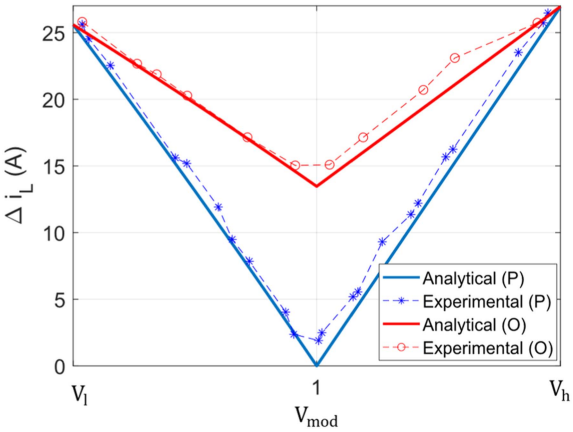

FIGURE 17. Inductor's current ripple experimental results.

The resulting waveforms from the experiments are shown in Fig. 18. The voltage across the inductor can be observed (V_{AB}) in green, and the current across the inductor (i_L) is also represented in light blue.

It can be observed that for figures A, B, and C, the maximum voltage is V_{in} and the minimum $-V_{out}$, and for the rest of the period, the voltage is equal to $V_{in} - V_{out}$. Since the analysis is performed in the buck–boost region, these two values are very close to each other, and the difference is very small.

For the other images D, E, F, the voltage across the inductor has a smaller span, in D the minimum value is still $-V_{out}$ but the positive V_{in} peak has been erased. Again, for the rest of the period the voltage is $V_{in} - V_{out}$ leaving a very small value. This means that the voltage withstanded by the inductor with the proposed strategy is much smaller, and thus, the current ripple diminishes.

This is the same scenario for figure F, where the negative part has been cancelled, and only the V_{in} peak remains. Notice that in this case $V_{in} - V_{out}$ is negative, ensuring that the average voltage across the inductor is equal to 0.

Finally, in E, both positive and negative peaks have been canceled, and since $V_{in} = V_{out}$ the voltage across the inductor is constant and equal to 0; as expected, the current ripple in this case is negligible.

Analyzing the current, the proposed modulation reduces the current ripple in all cases, since the voltage span supported by the inductor is smaller under the proposed modulation. The closer V_{out} is to V_{in} the greater the reduction is, around 14 A for this case, when $V_{in} = V_{out}$.

Therefore, when the input voltage is equal to the output voltage ($V_{mod} = 1$), the ripple is reduced to almost zero, as expected, thus improving the losses in the inductor. The current ripple is not exactly zero due to the small dead time in the switching signals needed for the practical implementation. Then, it can be seen that the ripple effect has been significantly reduced.

When analyzing the maximum current, the proposed modulation delivers a lower peak value. It can be observed that the current reduces from 27 A to 24 A in step-down mode, from

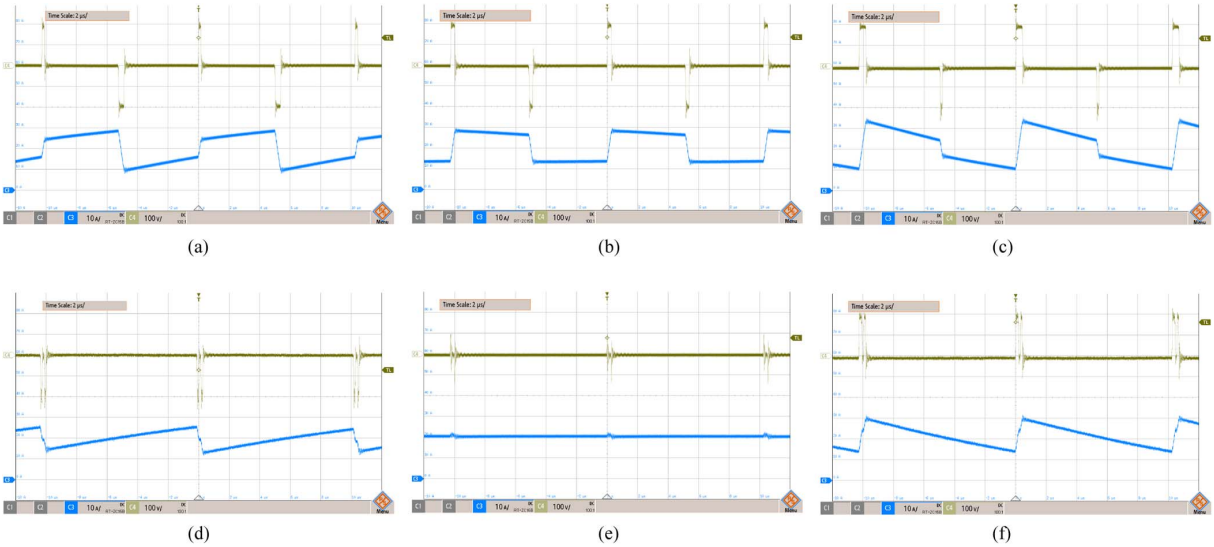

FIGURE 18. Experimental results waveforms ($V_{in} = 200$ V; $P_{out} = 4$ kW). Green = Inductor voltage, v_{AB}; light blue = Inductor current, i_l. (a) Original modulation ($V_{out} = 195$ V). (b) Original modulation ($V_{out} = 200$ V). (c) Original modulation ($V_{out} = 205$ V). (d) Proposed modulation ($V_{out} = 195$ V). (e) Proposed modulation ($V_{out} = 200$ V). (f) Proposed modulation ($V_{out} = 205$ V).

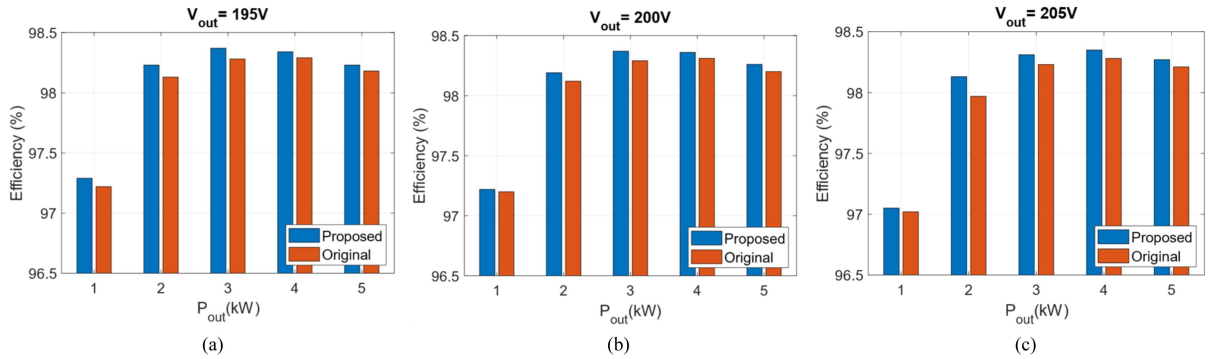

FIGURE 19. Efficiency comparison between the original modulation in red and the proposed modulation in blue for $V_{in} = 200$ V.

33 A to 28 A in step-up conditions, and from 30 A to 20 A when $V_{in} = V_{out}$.

This implies that, for the same application, under the proposed modulation, the inductance will withstand a lower maximum current, up to 33% lower in this case.

Finally, a comparative efficiency analysis was performed to validate the impact of the proposed modulation on the converter's overall losses. These efficiency measurements were acquired using a high-precision YOKOGAWA WT300 wattmeter. Fig. 19 presents the measured efficiency curves for both the original and proposed strategies, plotted across all tested operating points.

The results show an improvement, with the proposed method achieving a peak efficiency gain of 0.16% at $V_{out} = 205$ and $P_{out} = 2$ kW. More importantly, this data provides a crucial validation: it confirms that the significant advantages of the proposed strategy are achieved without any negative tradeoffs or penalties to the converter's overall efficiency.

The proposed modulation is presented as an enhanced strategy over the baseline method, offering significant advantages with minimal implementation complexity. The modification is very simple (requiring only a change from (63) to (64)), yet it yields benefits for the final implementation, design, and overall system efficiency. Furthermore, it reduces the maximum inductor current in the buck–boost region. Crucially, these gains are achieved without introducing negative side-effects or performance tradeoffs, with the minor exception (as previously discussed) related to specific t_{on}, t_{off}.

VII. CONCLUSION

The main focus of this work has been to analyze and improve the performance of the FSBB converter. The central contribution of this article is the proposal of a modified modulation strategy that sets a fixed 180° phase shift between the two bridges in the buck–boost operating region. This approach relies on the fact that the phase angle is an independent variable that does not affect the static voltage gain or the system's dynamics. Consequently, the proposed method exploits this additional degree of freedom to optimize the current

waveforms without altering the system's fundamental input–output relationship.

The results demonstrate that this strategy is highly effective in improving the converter's behavior. Both theoretical analysis and laboratory tests confirm that the new modulation consistently minimizes the inductor current ripple across the buck–boost region when compared to standard methods. In addition, it successfully reduces the peak inductor current, helping keep the magnetic components farther from saturation. Crucially, this improvement in current quality does not negatively impact the converter's efficiency. In fact, the experimental data show that the efficiency remains stable and even improves slightly, ensuring that the stress reduction is achieved without a power penalty.

From a practical point of view, the most significant benefit of this proposal is its simplicity. The superior performance is achieved through a minor adjustment to the modulator implementation, which can be easily implemented in standard digital control platforms without increasing the computational cost. Unlike other optimization techniques, which often require complex adaptive algorithms or additional hardware components, this method relies solely on a single operation change: replacing an addition with a subtraction. This makes the proposed modulation an attractive, robust, and cost-effective solution that can be applied directly to existing FSBB designs, providing an immediate performance upgrade with minimal engineering effort.

APPENDIX

The rms currents (35), (36), and (37) are further expanded for a better comprehension

$$I^2_{L_{\text{rms},O}} = I^2_L + \frac{V^2_{\text{in}} V^2_{\text{out}} V_h \left(V_h^2 - 3V_l^2\right) + V_l^3 V_{\text{out}} V_{\text{in}} \left(V^2_{\text{in}} + V^2_{\text{out}}\right)}{12\, V_h^3\, L^2\, f^2\, (V_{\text{in}} + V_{\text{out}})^2} \tag{65}$$

$$I^2_{L_{\text{rms},P}} = \begin{cases} I^2_L + \frac{V^2_{\text{out}}\, V_{\text{in}}\, (V_{\text{in}} - V_{\text{out}})^2\, V^3_{\text{max}}}{12\, V_h^3\, L^2\, f^2\, (V_{\text{in}} + V_{\text{out}})^3}, & V_{\text{in}} > V_{\text{out}} \\ I^2_L + \frac{V_{\text{out}}\, V^2_{\text{in}} (V_{\text{in}} - V_{\text{out}})^2\, V^3_{\text{max}}}{12\, V_h^3\, L^2\, f^2\, (V_{\text{in}} + V_{\text{out}})^3}, & V_{\text{in}} \leq V_{\text{out}}. \end{cases} \tag{66}$$

REFERENCES

[1] C.-W. Chen and Y.-M. Chen, "Analysis of the series-connected distributed maximum power point tracking PV system," in *Proc. IEEE Appl. Power Electron. Conf. Expo.*, Mar. 2015, pp. 3083–3088, doi: 10.1109/APEC.2015.7104791.

[2] M. Kasper, D. Bortis, T. Friedli, and J. W. Kolar, "Classification and comparative evaluation of PV panel integrated DC-DC converter concepts," in *Proc. IEEE 15th Int. Power Electron. Motion Control Conf.*, Sep. 2012, pp. LS1e.4–1–LS1e.4–8, doi: 10.1109/EPEPEMC.2012.6397403.

[3] M. Orellana, S. Petibon, B. Estibals, and C. Alonso, "Four switch buck-boost converter for photovoltaic DC-DC power applications," in *Proc. 36th Annu. Conf. IEEE Ind. Electron. Soc.*, Nov. 2010, pp. 469–474, doi: 10.1109/IECON.2010.5674983.

[4] X. Chen, A. A. Pise, J. Elmes, and I. Batarseh, "Ultra-highly efficient low-power bidirectional cascaded buck-boost converter for portable PV-battery-devices applications," *IEEE Trans. Ind. Appl.*, vol. 55, no. 4, pp. 3989–4000, Jul./Aug. 2019, doi: 10.1109/TIA.2019.2911566.

[5] M. Schulz, N. Schleippmann, K. Gosses, R. Chacon, and B. Wunder, "Four switch buck/boost converter to handle bidirectional power flow in DC subgrids," in *Proc. PCIM Europe Digit. Days 2020; Int. Exhib. Conf. Power Electron., Intell. Motion, Renewable Energy Energy Manage.*, Jul. 2020, pp. 1–8.

[6] C. L. Espinosa, "Asynchronous non-inverter buck-boost DC to DC converter for battery charging in a solar MPPT system," in *Proc. IEEE URUCON*, Oct. 2017, pp. 1–4, doi: 10.1109/URUCON.2017.8171863.

[7] D. Rezzak, A. Sitayeb, Y. Houam, K. Touafek, and N. Boudjerda, "A new design of lead-acid battery charger based on non-inverting buck-boost converter for the photovoltaic application," in *Proc. 6th Int. Renewable Sustain. Energy Conf.*, Dec. 2018, pp. 1–7, doi: 10.1109/IRSEC.2018.8703034.

[8] C. P. Mehta and P. Balamurugan, "Buck-boost converter as power factor correction controller for plug-in electric vehicles and battery charging application," in *Proc. IEEE 6th Int. Conf. Power Syst.*, Mar. 2016, pp. 1–6, doi: 10.1109/ICPES.2016.7584111.

[9] H.-S. Lee and J.-J. Yun, "High-efficiency bidirectional buck–boost converter for photovoltaic and energy storage systems in a smart grid," *IEEE Trans. Power Electron.*, vol. 34, no. 5, pp. 4316–4328, May 2019, doi: 10.1109/TPEL.2018.2860059.

[10] M. Schulz, N. Schleippmann, K. Gosses, B. Wunder, and M. März, "Four switch buck/boost converter for DC microgrid applications," in *Proc. 22nd Eur. Conf. Power Electron. Appl.*, Sep. 2020, pp. 1–10, doi: 10.23919/EPE20ECCEEurope43536.2020.9215754.

[11] L. Tai, M. Lin, J. Wang, and C. Hou, "Synchronous control strategy with input voltage feedforward for a four-switch buck-boost converter used in a variable-speed PMSG energy storage system," *Electronics*, vol. 10, no. 19, Jan. 2021, Art. no. 19, doi: 10.3390/electronics10192375.

[12] N. Kunstbergs, H. Hinz, N. Schofield, and D. Roll, "Efficiency improvement of a cascaded buck and boost converter for fuel cell hybrid vehicles with overlapping input and output voltages," *Inventions*, vol. 7, no. 3, Sep. 2022, Art. no. 74, doi: 10.3390/inventions7030074.

[13] Z. Guo and T. Mao, "Efficiency optimization and control strategy of four-switch buck-boost converter for wide conversion ratio," *IEEE Trans. Power Electron.*, vol. 38, no. 9, pp. 10702–10715, Sep. 2023, doi: 10.1109/TPEL.2023.3282203.

[14] Z. Yu, H. Kapels, and K. F. Hoffmann, "High efficiency bidirectional DC-DC converter with wide input and output voltage ranges for battery systems," in *Proc. Int. Exhib. Conf. Power Electron., Intell. Motion, Renewable Energy Energy Manage.*, May 2015, pp. 1–8.

[15] X. Ren, X. Ruan, H. Qian, M. Li, and Q. Chen, "Dual-edge modulated four-switch Buck-Boost converter," in *Proc. IEEE Power Electron. Specialists Conf.*, Jun. 2008, pp. 3635–3641, doi: 10.1109/PESC.2008.4592520.

[16] Q. Ullah, X. Wu, and U. Saleem, "Current controlled robust four-switch buck-boost DC-DC converter," in *Proc. Int. Conf. Comput., Electron. Elect. Eng.*, Oct. 2021, pp. 1–6, doi: 10.1109/ICECube53880.2021.9628275.

[17] N. Zhang, S. Batternally, K. C. Lim, K. W. See, and F. Han, "Analysis of the non-inverting buck-boost converter with four-mode control method," in *Proc. IEEE 43rd Annu. Conf. Ind. Electron. Soc.*, Oct. 2017, pp. 876–881, doi: 10.1109/IECON.2017.8216151.

[18] S. Waffler and J. W. Kolar, "A novel low-loss modulation strategy for high-power bidirectional buck + boost converters," *IEEE Trans. Power Electron.*, vol. 24, no. 6, pp. 1589–1599, Jun. 2009, doi: 10.1109/TPEL.2009.2015881.

[19] Q. Liu, Q. Qian, B. Ren, S. Xu, W. Sun, and H. Li, "A new modulation strategy for four-switch buck-boost converter with reduced freewheeling current," in *Proc. IEEE Appl. Power Electron. Conf. Expo.*, Mar. 2020, pp. 2104–2108, doi: 10.1109/APEC39645.2020.9124107.

[20] Y. Bai, Y. Cao, V. Mitrovic, B. Fan, R. Burgos, and D. Boroyevich, "A simplified quadrangle current modulation for four-switched buck-boost converter (FSBB) with a novel small signal model," in *Proc. IEEE Appl. Power Electron. Conf. Expo.*, Mar. 2023, pp. 736–743, doi: 10.1109/APEC43580.2023.10131331.

[21] E. Gallo, D. Biadene, F. Cvejić, G. Spiazzi, and T. Caldognetto, "An energy-based model of four-switch buck–boost converters," *IEEE Trans. Power Electron.*, vol. 39, no. 4, pp. 4139–4148, Apr. 2024, doi: 10.1109/TPEL.2023.3349327.

[22] X. Ren, X. Ruan, H. Qian, M. Li, and Q. Chen, "Three-mode dual-frequency two-edge modulation scheme for four-switch buck–boost converter," *IEEE Trans. Power Electron.*, vol. 24, no. 2, pp. 499–509, Feb. 2009, doi: 10.1109/TPEL.2008.2005578.

[23] Y. Wang, J. Lan, X. Huang, T. Fang, X. Ruan, and M. Dong, "An improved single-mode control strategy based on four-switch buck-boost converter," in *Proc. IEEE Appl. Power Electron. Conf. Expo.*, Mar. 2020, pp. 320–325, doi: 10.1109/APEC39645.2020.9124612.
[24] L. Callegaro, M. Ciobotaru, D. J. Pagano, E. Turano, and J. E. Fletcher, "A simple smooth transition technique for the noninverting buck–boost converter," *IEEE Trans. Power Electron.*, vol. 33, no. 6, pp. 4906–4915, Jun. 2018, doi: 10.1109/TPEL.2017.2731974.
[25] H. Qin, Y. Yang, S. Xie, W. Chen, J. Peng, and D. Fu, "Mechanisim of duty cycle mutation and a new mode smooth switching control method in high efficiency four-mode four-switch buck-boost converter," in *Proc. Int. Conf. Power Energy Syst. Appl.*, Feb. 2022, pp. 304–311, doi: 10.1109/ICoPESA54515.2022.9754390.
[26] I. Aharon, A. Kuperman, and D. Shmilovitz, "Analysis of dual-carrier modulator for bidirectional noninverting buck–boost converter," *IEEE Trans. Power Electron.*, vol. 30, no. 2, pp. 840–848, Feb. 2015, doi: 10.1109/TPEL.2014.2315993.
[27] Y.-J. Lee, A. Khaligh, and A. Emadi, "A compensation technique for smooth transitions in a noninverting buck–boost converter," *IEEE Trans. Power Electron.*, vol. 24, no. 4, pp. 1002–1015, Apr. 2009, doi: 10.1109/TPEL.2008.2010044.
[28] V. Díaz, A. Barrado, A. Lázaro, and P. Zumel, "Comparison of several modulation strategies for the four Switch buck-boost converter," in *Proc. IEEE 17th Int. Conf. Compat., Power Electron. Power Eng.*, Tallinn, Estonia: IEEE, Jun. 2023, pp. 1–6, doi: 10.1109/CPE-POWERENG58103.2023.10227467.
[29] V. Díaz, A. Barrado, A. Lázaro, and P. Zumel, "An improved modulation strategy for a four-switch buck-boost converter with reduced current ripple," in *Proc. Int. Conf. Clean Elect. Power*, Jun. 2023, pp. 154–160, doi: 10.1109/ICCEP57914.2023.10247450.
[30] X. Nan and C. R. Sullivan, "An improved calculation of proximity-effect loss in high-frequency windings of round conductors," in *Proc. IEEE 34th Annu. Conf. Power Electron. Specialist*, Jun. 2003, vol. 2, pp. 853–860, doi: 10.1109/PESC.2003.1218168.
[31] A. Reatti and M. K. Kazimierczuk, "Comparison of various methods for calculating the AC resistance of inductors," *IEEE Trans. Magn.*, vol. 38, no. 3, pp. 1512–1518, May 2002, doi: 10.1109/20.999124.

VICTOR DIAZ received the B.S. degree in industrial electronics and automation engineering and the M.S. degree in electronic systems engineering in 2020 and 2021, respectively, from the University Carlos III of Madrid, Getafe, Spain, where he is currently working toward the Ph.D. degree in electronic engineering with the Power Electronics Systems Group.

His research interests include dc–dc switching power converters design, modeling and optimization of modulation strategies, and power distribution systems optimization for hydrogen-powered vehicles and drones.

ANDRES BARRADO (Senior Member, IEEE) received the M.Sc. degree in electrical engineering from Polytechnic University of Madrid, Madrid, Spain, in 1994, and the Ph.D. degree in electrical engineering from Carlos III University of Madrid, Getafe, Spain, in 2000.

He is a Full Professor with the Carlos III University of Madrid since 2012, and the Head of the Power Electronics Systems Group since 2004. He has authored and coauhtored more than 230 scientific papers in international journals and conference proceedings and holds 12 patents. He has been actively involved in over 100 R&D projects for companies in Europe and the U.S, and more than 33 projects with public funding, in the field of power electronics. He is a co-founder of the spin-off company "Power Smart Control S.L.", focused on applications in power electronics. His research interests include bidirectional dc–dc converters, solar, and fuel cell conditioning, behavioral modeling of converters and systems, hydrogen-powered electric vehicles and drones, power distribution systems for aircraft, and electromagnetic compatibility.

PABLO ZUMEL (Member, IEEE) received the B.S. degree in electrical engineering from the University of Burgos, Burgos, Spain, in 1995, the first M.S. degree in electrical engineering from the Universidad Politécnica de Madrid (UPM), Madrid, Spain, in 1999, the second M.S. degree in electrical engineering from the Ecole Centrale Paris, Paris, France, in 2000, and the Ph.D. degree in electrical engineering from UPM in 2005.

From 1999 to 2003, he was a Researcher with the UPM. Since 2003, he has been with the Department of Electronic Technology, Carlos III University of Madrid, Leganés, Spain, where he is currently a Full Professor. He has authored/coauthored more than 100 scientific papers in main international conferences and journals, has filed four patents, and is the co-founder of a spin-off company targeting CAD for power electronics. He has participated in more than 50 research projects in the field of power electronics. His research interests include digital control in power electronics, modeling and control techniques, modular power converters, design optimization, and educational topics in power electronics.

ANTONIO LAZARO (Member, IEEE) was born in Madrid, Spain, in 1968. He received the M.Sc. degree in electrical engineering from the Universidad Politécnica de Madrid, Madrid, Spain, in 1995 and the Ph.D. degree in electrical engineering from the Universidad Carlos III de Madrid, Getafe, Spain, in 2003.

He has been a Full Professor with the Universidad Carlos III de Madrid since 1995. He has been involved in power electronics since 1994, participating in more than 80 research and development projects for industry. He holds 11 patents and software registrations, and he has published nearly 150 papers in IEEE journals and conferences. He is co-founder of Power Smart Control S.L. His research interests include design and optimization of medium and high-power dc–dc converters, power factor correction rectifiers, inverters (railway and grid-tied applications), advanced modulation techniques, modeling, and digital control of switching converters.